MATERIALS SCIENCE

Molecular-caged metal-organic frameworks for energy management

Minghong Wu[1], Gengye Lin[1], Rui Li[1], Xing Liu[1], Shumei Liu[1], Jianqing Zhao[1]*, Weiqi Xie[2]*

Metal-organic frameworks (MOFs) hold great promise for diverse applications when combined with polymers. However, a persistent challenge lies in the susceptibility of exposed MOF pores to molecule and polymer penetration, compromising the porosity and overall performance. Here, we design a molecular-caged MOF (MC-MOF) to achieve contracted window without sacrificing the MOF porosity by torsional conjugated ligands. These molecular cages effectively shield against the undesired molecule penetration during polymerization, thereby preserving the pristine porosity of MC-MOF and providing outstanding light and thermal management to the composites. The polymer containing 0.5 wt % MC-MOF achieves an 83% transmittance and an exceptional haze of 93% at 550 nanometers, coupled with remarkable thermal insulation. These MC-MOF/polymer composites offer the potential for more uniform daylighting and reduced energy consumption in sustainable buildings when compared to traditional glass materials. This work delivers a general method to uphold MOF porosity in polymers through molecular cage design, advancing MOF-polymer applications in energy and sustainability.

INTRODUCTION

Compositing metal-organic frameworks (MOFs) with polymers provides a versatile platform for various applications (*1*). Now, MOF-polymers are prepared by different methods such as MOF blending with polymers, covalent grafting of polymers, growth of MOF on polymer templates, and in situ polymerization with MOF (*2*, *3*). Nevertheless, a longstanding challenge arises from the exposed MOF pores, which are susceptible to penetration by small molecules like monomers and curing agents or even polymer interpenetration, leading to the reduced MOF porosity and compromised performance of MOF-polymers (*4*–*6*).

Current approaches have often revolved around the selection of MOFs with small pores, such as UiO-66 (*7*, *8*) or ZIF-8 (*9*), as a means of avoiding the undesired molecule penetration. However, this strategy has inherent limitations as it is not universally applicable across the diverse spectrum of MOFs. Highly porous MOFs prepared with large ligands typically provide better performance in polymers. Paradoxically, these large ligands also result in wider exposed windows, making MOFs more susceptible to molecule penetration, consequently sacrificing their porosity in polymers. Thus, the development of a general strategy to maintain MOFs' high porosity is of great importance, as it has the potential to unlock additional horizons for MOF-polymer applications in energy management (*10*).

Energy management, such as light harvesting and thermal regulation, holds substantial promise in diverse fields, from photovoltaic devices (*11*, *12*) to sustainable buildings (*13*, *14*). Light harvesting materials, for example, are typically transparent in the visible range and strongly scatter in the forward direction (*15*, *16*). MOF-polymers present an intriguing avenue for light harvesting due to the unique characteristics of MOFs, featuring metal clusters and high porosity, which engender multiple scattering mechanisms. These materials offer additional benefits of controlling particle size for enhanced forward scattering (*17*), versatile structural design, and ease of synthesis (*18*). When compositing MOFs with polymers, the pivotal role played by MOF pore structures in enabling efficient light scattering underscores the paramount importance of preserving MOF porosity in polymers. Therefore, a general strategy for impeding molecule penetration is required to open unexplored frontiers for the application of MOF-polymers in sustainable energy.

Here, we have pioneered the concept of molecular-caged MOFs (MC-MOF) through ligand engineering, in which the contraction of the MC-MOF windows is realized by torsional conjugated ligands without sacrificing the porosity. This innovative approach leverages molecular cages to efficiently counter the penetration of molecules and polymers, thereby safeguarding high porosity of MC-MOFs and optimizing their performance in polymer matrices. Our work demonstrates the efficiency and universality of the molecular cage effect through a combination of experiments and simulations. The resulting MC-MOF epoxy-based material [Zr–9,10-di(p-carboxyphenyl) anthracene (DPA)/EP] shows an ultrahigh haze (93%, 550 nm) with a light transmittance of 83% (550 nm) at a low MC-MOF loading of 0.5 wt %. Zr-DPA/EP also provides a wide ultraviolet (UV) shielding and UV fluorescence response with a low thermal conductivity of 0.16 W m^{-1} K^{-1}. Moreover, our exploration extends to the domain of sustainable building applications, where Zr-DPA/EP outperforms conventional glass by yielding a more uniform distribution of daylighting and reducing energy consumption. The design principle, in which molecular cages are constructed through ligand engineering, delivers an optimal solution for MOF to maintain high porosity in polymers and foster fresh vistas for their application in energy management.

RESULTS

Design and synthesis of MC-MOF

Ligand engineering is an efficient strategy to modulate the pore structures of MOF, for example, UiO-68 with a larger ligand ([p-terphenyl]-4,4″-dicarboxylic acid, TPDC) has higher porosity and specific surface area than its counterparts in the series (UiO-66 and UiO-67; fig. S1), which can result in a more efficient scattering effect when coupled with polymer matrices (*19*). However, the excessively

[1]School of Materials Science and Engineering, Key Laboratory Guangdong High Property and Functional Polymer Materials, Plant Fiber Material Science Research Center, State Key Laboratory of Pulp and Paper Engineering, South China University of Technology, Guangzhou 510640, China. [2]School of Minerals Processing and Bioengineering, Central South University, Changsha 410083, China.
*Corresponding author. Email: weiqixie@csu.edu.cn (W.X.); psjqzhao@scut.edu.cn (J.Z.)

large ligands may suffer from the formation of network interpenetration and the decrease of MOF stability, as well as the high cost and the increased difficulty of synthesis (*20*). Given the high stability of various Zr-based MOFs and the minimal impact of white $ZrCl_4$ on optical sample coloration, UiO-68 synthesized from $ZrCl_4$ and TPDC (Fig. 1A) is a promising candidate for preparing MOF-polymer colorless optical materials with high transmittance and high haze.

The inherent high porosity of UiO-68 always comes with a vulnerability to molecule and polymer penetration, primarily due to the exposure of sizable windows (greater than 10 Å), resulting in a sacrifice of porosity. This issue is a common challenge encountered when incorporating UiO-68 into most polymer matrices, and it becomes even more pronounced in the case of crosslinked polymers prepared from small molecules, such as epoxy resins (EPs). This heightened susceptibility is a consequence of the necessity to introduce MOFs before curing, leaving them unavoidably exposed to small compounds, mainly curing agents and prepolymers. To address this, we develop the concept of MC-MOF through torsional conjugated ligands. Specifically, the TPDC ligand of UiO-68 is replaced with DPA to synthesize MC-MOF (Zr-DPA; Fig. 1B). In this unique design, the expansive conjugation planes of the anthracene structure are contorted at a large angle (fig. S2A), resulting in the contraction of the MOF's window while upholding its remarkable porosity.

The rational design of ligands also plays a pivotal role, necessitating considerations of side groups, color attributes, and cost effectiveness. The widely used ligand, 2′-amino-[1,1′:4′,1″-terphenyl]-4,4″-dicarboxylic acid (fig. S2B), falls short of being an optimal choice due to the relatively small amino group, which fails to provide an effective barrier effect. In contrast, a large and planar benzene ring represents a more promising option. In addition, the precise linkage of the benzene ring is of great importance. Compared to the conjugated anthracene structure observed in DPA, the side group of 2′,5′-diphenyl-[1,1′:4′,1″-terphenyl]-4,4″-dicarboxylic acid (fig. S2C) is connected via a C—C single bond, resulting in the rotation of the side benzene ring, rendering it ineffective as a robust barrier (*21*). Consequently, ligands with conjugated benzene rings emerge as the preferred choice. Nevertheless, excessively large conjugation tends to impart a dark color to the ligand. For instance, the anthracene-containing DPA ligand exhibits an off-white hue, while the 5,12-diphenyl-tetracenedicarboxylate (fig. S2D) ligand, featuring a larger conjugated side group, assumes an orange hue, making it unsuitable for applications in optical materials (*22*). Therefore, the commercially available DPA ligand stands out as the optimal candidate for synthesizing MC-MOF.

Nanoparticles with Mie scattering effect stand as auspicious candidates for the conferment of high haze and transmittance to materials, given their propensity to invoke forward scattering (*23*). Mie scattering theory is applied to guide the regulation of MOF particle sizes, and a common strategy entails the addition of modulators to exert precise control over the morphology and particle sizes of Zr-based MOFs (*24*). Therefore, trifluoroacetic acid (TFA) was used to modulate both UiO-68 and Zr-DPA. Scanning electron microscopy

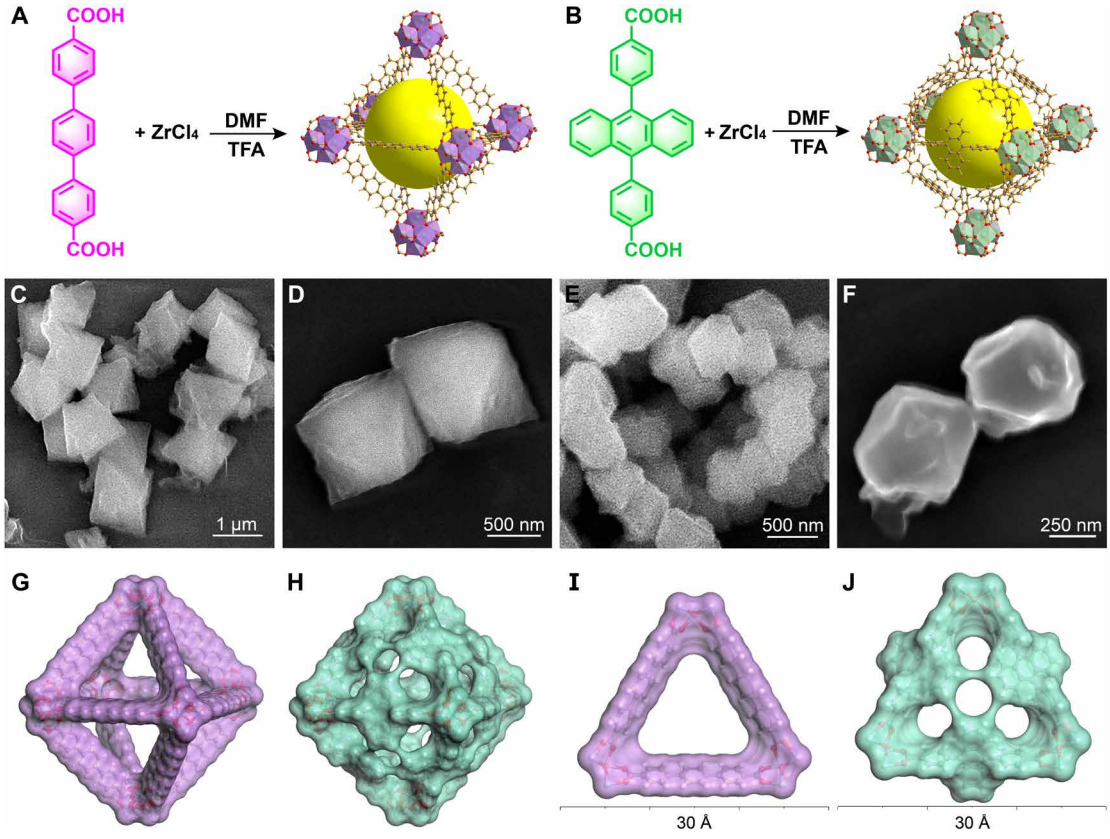

Fig. 1. Design and synthesis of MC-MOF. Synthetic routes of (**A**) UiO-68 and (**B**) Zr-DPA. (**C** and **D**) SEM images of UiO-68. (**E** and **F**) SEM images of Zr-DPA. Pore structures of (**G**) UiO-68 and (**H**) Zr-DPA with Connoly surfaces. Window structures of (**I**) UiO-68 and (**J**) Zr-DPA with Connoly surfaces.

(SEM) results show that the particle size of UiO-68 (Fig. 1, C and D) is around 1 μm, compared to that of Zr-DPA (Fig. 1, E and F) around 600 nm under the same synthesis conditions. The distribution range of particle size is further determined using a dynamic light scattering method. UiO-68 predominantly exhibits a distribution spanning from 700 to 1300 nm, with a peak centering at approximately 1 μm (fig. S3), characteristics that harmoniously echo the SEM results. In comparison, the particle distribution of Zr-DPA predominantly spans from 400 to 800 nm, spanning the entire spectrum of visible light, with a notable peak centered around 600 nm (fig. S4). Grounded in the fundamental principles of Mie scattering, this modulation of particle sizes engenders a potent forward scattering effect with high scattering intensity. The x-ray diffraction (XRD) analysis, illustrated in figs. S5 and S6, confirms the high crystallinity of the synthesized UiO-68 and Zr-DPA and is similar to the simulated XRD spectra. Further structural characterization through Fourier transform infrared (FTIR) spectroscopy, as depicted in fig. S7, offers additional verification of the successful MOF synthesis.

Molecular cage effect of MC-MOF

The molecular cage of MC-MOF allows for efficient window contraction without sacrificing the intrinsic high porosity. Figure 1 (G and H) shows the frameworks of UiO-68 and Zr-DPA with Connoly surfaces. The large conjugate planes of anthracene primarily influence the window position rather than the internal MOF pore structure, fostering the expectation that Zr-DPA would uphold a commendable level of porosity. This is verified by N_2 adsorption and desorption tests, revealing Brunauer-Emmett-Teller surface areas of 2823 m^2/g for UiO-68 (fig. S8) and 2701 m^2/g for Zr-DPA (fig. S9). These results provide evidence that Zr-DPA retains a high level of porosity akin to that of UiO-68, showing that the construction of molecular cages does not entail substantial sacrifices in porosity. For a closer examination of the window structures, as shown in Fig. 1 (I and J) , UiO-68 exhibits triangular windows exceeding 10 Å in size, permitting the entry of small molecules like epoxy curing agents (Fig. 2A). In contrast, the window of Zr-DPA, owing to the presence of the torsional anthracene structure, is divided into four contracted windows measuring approximately 5 Å each. This particular window size, while accommodating the passage of N_2, effectively acts as a barrier to the epoxy curing agent, thus upholding the high porosity of Zr-DPA in polymer matrices (Fig. 2B).

To demonstrate the versatility of the strategy, the three-dimensional molecular sizes of nine commonly used anhydride curing agents are calculated (fig. S10). This assessment reveals that the sizes of the majority of these curing agents fall within the range of 5 to 10 Å. These dimensions, while allowing for access to the wide windows of UiO-68, are obstructed by the contracted windows of Zr-DPA. Among these curing agents, methylhexahydrophthalic anhydride (MHHPA) emerges as the ideal candidate for our subsequent experiments because it not only has the appropriate molecular size but also is a transparent and colorless liquid at room temperature, thereby affording exceptional operational stability and facilitating the preparation of optical samples. Beyond these advantages, the utilization of potentially hazardous organic solvents is effectively eradicated due to MHHPA's liquid state, thereby eliminating any concerns of solvent infiltration into the MOF's pore structures.

Porosity changes of MOF in polymer systems are evaluated by gas permeation tests. As listed in table S1, the gas transmission rate of Zr-DPA/EP is much larger than that of UiO-68/EP and pure EP, suggesting that the MC-MOF maintains a higher porosity in the polymer. Theoretical insights into the molecular cage effect have been further revealed using density functional theory (DFT) calculations. We computed the minimum energy paths for the diffusion of MHHPA molecules in UiO-68 (Fig. 2C) and Zr-DPA (Fig. 2D), respectively. The results (Fig. 2E) show that the energy barrier of MHHPA in UiO-68 is 0.18 eV, whereas it is increased to 0.34 eV in Zr-DPA, which is almost doubled. This indicates that the molecular cage of Zr-DPA can efficiently inhibit the penetration of curing agent and maintain porosity.

Optical properties of MC-MOF/polymer

Epoxy resins are commercially available as building materials for construction industries and encapsulation layers for optoelectronic devices due to their high light transmission, remarkable thermal stability, and impressive mechanical properties, which render EPs an ideal candidate for the preparation of light harvesting materials with MOFs. Figure 2F visually illustrates the dispersion of UiO-68 and Zr-DPA, where the near-white color meets the basic requirements for optical materials. Thus, they are introduced into EPs to prepare light management materials with forward scattering effect. (Fig. 2G).

Transmittance and haze, as fundamental parameters in optical materials, assume pivotal roles in architectural design. Transmittance provides adequate interior lighting, and haze allows for a more uniform daylight illuminance and avoids patches of sunlight. Figure 3A shows that pure EP exhibits a high transmittance in the visible spectrum from 400 to 800 nm, typically hovering around 90%. The introduction of 0.5 wt % MOF into the EPs, in the form of UiO-68/EP and Zr-DPA/EP composites, effectively preserves high overall transmittances, predominantly exceeding 70% across the visible spectrum. Specifically, the transmittance values at 550 nm demonstrate an 80% for UiO-68/EP and 83% for Zr-DPA/EP, showing their capacity to meet the fundamental lighting requisites that architectural design demands.

The measurement of haze serves as a valuable gauge of forward scattering. As illustrated in Fig. 3B, pure EP exhibits virtually negligible haze levels within the visible range. In contrast, the introduction of a mere 0.5 wt % MOF, while concurrently upholding high transmittance, causes a remarkable surge in the haze of the composites. The haze of UiO-68/EP decreases when increasing wavelength with a finite haze of 58% at 550 nm, which is attributed to the penetration of UiO-68 straight pores by molecules, leading to a reduction in overall porosity. Conversely, Zr-DPA/EP achieves haze levels that consistently surpassed 80% in the visible spectrum, notably outperforming UiO-68/EP, and reaching an exceptional haze value of 93% at 550 nm. Such a high transmittance and haze is attributed to several reasons: (i) The inherent high porosity of Zr-DPA provides a theoretically strong scattering. (ii) The molecular cages, acting as barriers against molecular penetration, allow Zr-DPA to uphold its high porosity and scattered efficiently within the polymer. (iii) The suitably tailored particle size of Zr-DPA induces an efficient Mie scattering effect.

In the realm of construction materials, prolonged exposure to intense sunlight necessitates the incorporation of effective UV shielding properties. Traditional materials, such as plastics and glass, often falter in their ability to block UVA radiation (320 to 400 nm), a substantial component of sunlight's UV spectrum, known for its ability to induce skin tanning and premature aging. Pure EPs, for example, have a fairly good barrier to UVB (290 to 320 nm) but fail to block

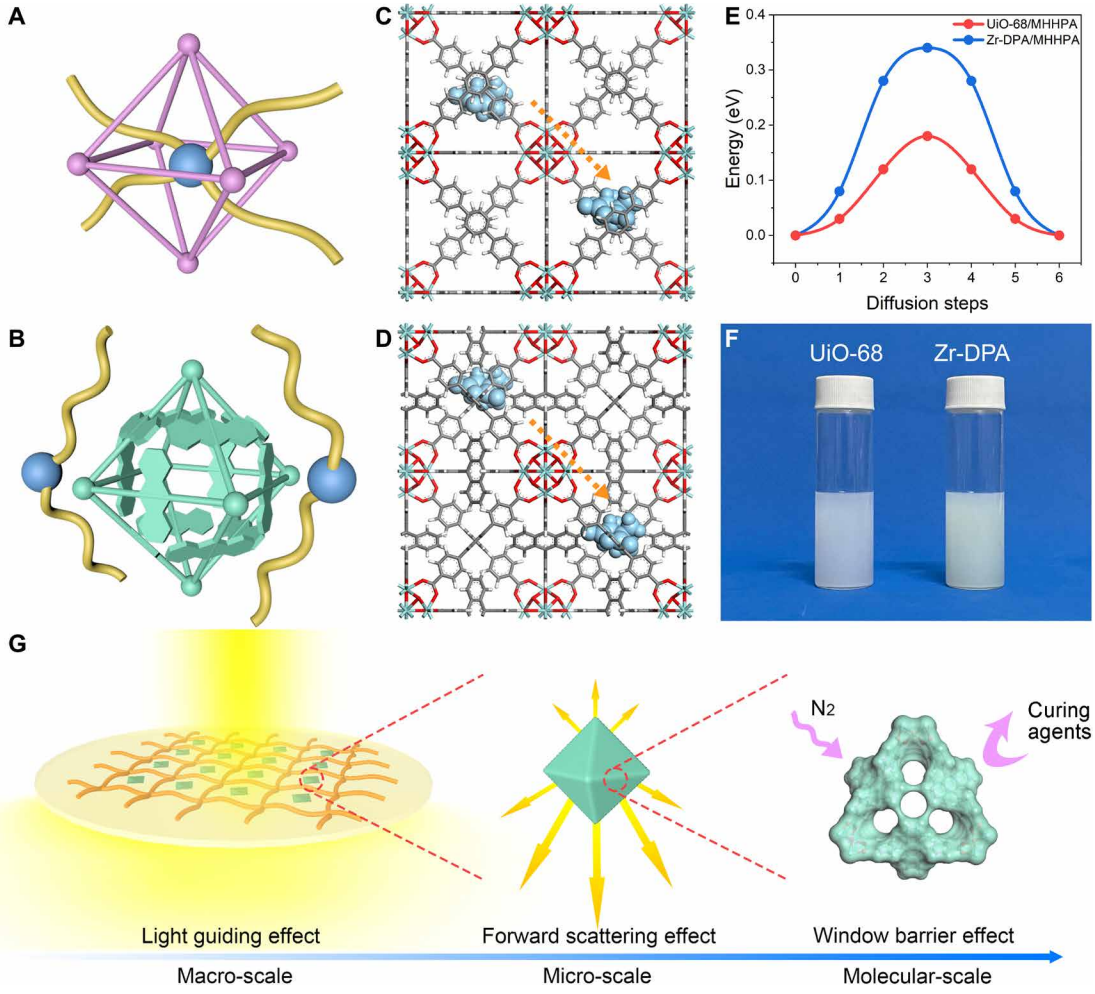

Fig. 2. Molecular cage effect of MC-MOF. (**A**) Possible interpenetrating structures of UiO-68 exposed pores and polymers, where the blue ball represents the curing agent and the yellow line represents the polymer chain. (**B**) Barrier effect of the molecular cage of Zr-DPA against the polymer. Diffusion of MHHPA (blue) in (**C**) UiO-68 and (**D**) Zr-DPA structures. (**E**) Energy barriers for the diffusion of MHHPA in UiO-68 and Zr-DPA. (**F**) Photograph of UiO-68 and Zr-DPA dispersions. (**G**) Diagram of Zr-DPA/EP light scattering mechanism.

most UVA as it still has 70% light transmission at 365 nm. Consequently, a pressing need arises to bolster UV shielding while preserving optimal visible light transmission. Here, a peak coupling method is proposed to construct a broad UV shielding platform by superimposing the characteristic peaks of MOF with the UV shielding band of EP. Zr-DPA/EP shows a higher absorbance in the UV region (300 to 400 nm) when compared to its counterparts, pure EP, and UiO-68/EP, indicating its remarkable UV shielding effect (Fig. 3C). Further insights into the process of constructing this UV shielding platform are elucidated in figs. S11 and S12. UiO-68 exhibits a characteristic peak around 360 nm, and through its coupling with EP, UiO-68/EP effectively extends its UV shielding abilities to encompass the wavelength range from 310 to 360 nm, with a transmittance of about 25%. However, it still remains insufficient for the comprehensive coverage of the entire UVA spectrum. The broader absorption peak centered around 410 nm in Zr-DPA, when combined with EPs, confers a substantial 100-nm-wide UV shielding band (ranging from 310 to 410 nm) in Zr-DPA/EP, resulting in a transmittance of less than 20%. This capacious protective range deftly encompasses the entire expanse of UVA, with minimal encroachment on visible light.

We also take optical photographs of EP, UiO-68/EP, and Zr-DPA/EP to visualize the changes in transmittance and haze using the method shown in Fig. 3D. When the samples are placed closely to the paper surface, they all display remarkable clarity, with the words "*MOF Haze*" easily discernible, a testament to their high transmittance (Fig. 3E). However, when the samples are positioned 1 cm above the paper surface, the text beneath the pure EP is still prominently discernible, revealing that pure EP is almost devoid of scattering effect. While the haze of UiO-68/EP modestly obscures the words, they remain partially visible. In comparison, Zr-DPA/EP exhibits a remarkable propensity for light scattering, entirely obscuring the text underneath, rendering even the color of the words imperceptible (Fig. 3F). These observations corroborate the high haze values of Zr-DPA/EP obtained through optical testing, further validating the tangible impact of the molecular cage effect. Furthermore, a comparative evaluation of light transmission and haze between Zr-DPA/EP and previously reported epoxy-containing

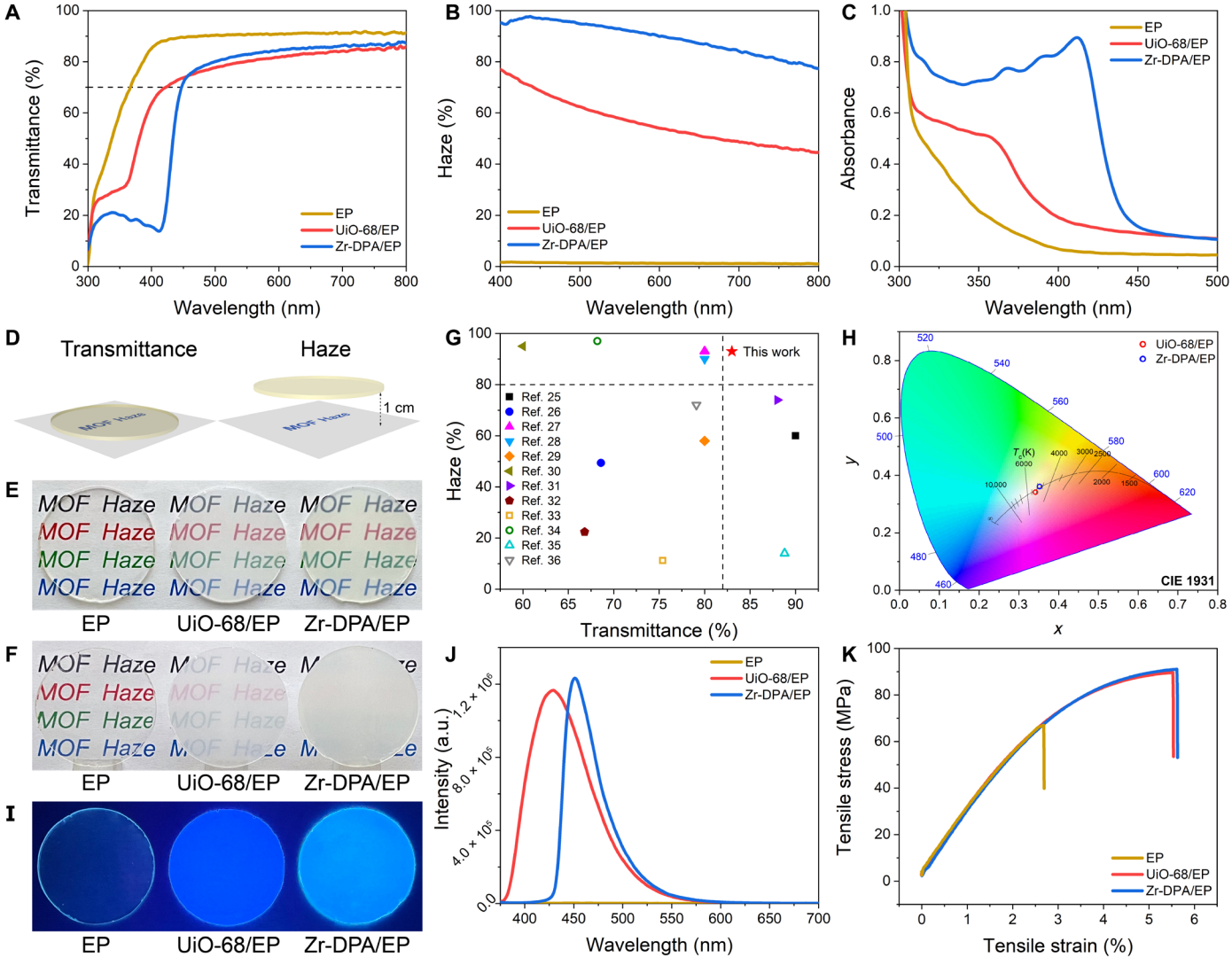

Fig. 3. Optical Properties of MC-MOF/polymer. (**A**) Transmittance, (**B**) haze, and (**C**) absorbance of MOF/EP. (**D**) Schematic diagram of transmittance and haze test. Optical photographs of MOF/EP (**E**) close to paper and (**F**) 1 cm away from the paper. (**G**) Comparison of Zr-DPA/EP in terms of haze and transmittance with previous work. (**H**) CIE chromaticity diagram with color temperature of Zr-DPA/EP and UiO-68/EP. (**I**) Photographs of MOF/EP under 365-nm UV excitation. (**J**) Fluorescence emission spectra of MOF/EP samples. (**K**) Mechanical properties of MOF/EP. a.u., arbitrary units.

optical materials (*25*–*36*) reaffirms the advantages of Zr-DPA/EP in both of these crucial aspects (Fig. 3G and table S2), positioning it as a highly promising material for architectural applications in light management.

The coloration of optical materials plays a pivotal role in various applications, especially in the realm of daylighting, where colorlessness is often sought to minimize visible light absorption and ensure high light transmission. Figure 3H shows the CIE chromaticity diagram and color temperature line of the samples. It is manifest that both UiO-68/EP and Zr-DPA/EP reside within the chromatic vicinity of white, a characteristic in harmony with their optical photos. Furthermore, the color temperatures of these specimens, approximately 5200 K for UiO-68/EP and 4800 K for Zr-DPA/EP, are proximate to the typical color temperature of midday sunlight (about 5000 K), rendering them suitable for daily lighting requisites. Distinctive character of MOFs, compared to traditional nanoparticle-mediated materials, lies in their amenability to tunability and functionalization. For example, the alteration of ligands offers a facile route to confer diverse photoluminescence properties upon MOFs. Figure 3I visually shows the fluorescence of the samples when subjected to 365-nm UV lamp excitation. UiO-68 and Zr-DPA exhibit dark blue and light blue fluorescence, respectively. The fluorescence emission spectra of the samples under 360-nm UV are compared in Fig. 3J. UiO-68/EP exhibits fluorescence with a peak centered at 430 nm, while Zr-DPA/EP shows a more pronounced fluorescence intensity characterized by a peak at 450 nm.

The mechanical properties of MOF-polymer composites are also investigated (Fig. 3K). Tensile tests reveal that the tensile strength of pure EP is 67 MPa, whereas UiO-68/EP and Zr-DPA/EP exhibit increased tensile strengths of around 90 MPa. The fracture elongations of MOF/EPs reach approximately 5.5%, about twice that of pure EP at 2.7%, without sacrificing modulus. This is primarily attributed to

the rigid framework structure of MOF, which not only contributes to the improvement of strength but also hinders and disperses crack propagation during the fracture of thermosets, known as the "crack pinning" effect, thereby enhancing toughness. In addition, the fracture surface morphologies of MOF-modified epoxy thermosets are observed through SEM. The fracture surface of UFT-0 is flat with only a few tiny cracks, indicating its typical brittle nature (fig. S13). In contrast, the fracture surface morphology of UiO-68/EP (fig. S14) and Zr-DPA/EP (fig. S15) becomes rough, with numerous crimped and mosaic flakes, demonstrating that MOF improves the toughness of epoxy thermosets, consistent with the results of mechanical tests. EDS mappings further reveal the distribution of C, O, and Zr elements, indicating that UiO-68 and Zr-DPA are uniformly dispersed in the epoxy matrix, which is advantageous for preparing large-scale, uniformly hazy MOF-polymer materials.

Light management of MC-MOF/polymer

The incorporation of MOF into the polymer matrix through in situ polymerization enables the preparation of extensive, homogeneous light management materials. As illustrated in fig. S16, the fabrication of a 10 cm by 10 cm by 1 mm Zr-DPA/EP large sample shows its potential for scalable production. Comparison of glass and Zr-DPA/EP in light management highlights the better performance of Zr-DPA/EP in practical applications. The optical properties of glass are shown in fig. S17. Evaluation of forward scattering is conducted through a laser irradiation test, wherein a 532-nm green laser passes through the sample and illuminates a white background plate positioned 20 cm away. The majority of the laser passed directly through the glass (Fig. 4A), resulting in tiny green dots on the background board (Fig. 4B), indicating minimal light scattering. In contrast, intense Mie scattering occurred in Zr-DPA/EP (Fig. 4C), with the laser exhibiting a large scattering angle that enveloped the entire background panel (covering an area of up to 1600 cm^2; Fig. 4D), providing evidence of the robust forward light scattering effect.

In the realm of architectural design, the haze materials serve to diffuse sunlight, mitigate discomfort glare, and foster comfortable, well-illuminated environments. (Fig. 4, E and F) This effect is demonstrated through the construction of a 15 cm by 15 cm by 15 cm house model with a lawn, upon which white parallel light is directed to simulate sunlight on a roof composed of either glass or Zr-DPA/EP. When the light traverses the glass, it illuminates only a small portion of the lawn, resulting in an uneven distribution of light intensity concentrated at the center, emanating a dazzling glare (Fig. 4G). Conversely, the application of Zr-DPA/EP yields an even and soft light distribution as the light is robustly scattered, fully illuminating the entire lawn (Fig. 4H). This observation suggests the potential of Zr-DPA/EP for daylighting applications and reducing indoor electricity consumption.

Thermal management of MC-MOF/polymer

Another crucial property of building materials, thermal management, plays a pivotal role in reducing energy consumption and maintaining comfortable indoor temperatures. However, conventional materials like glass, often used in architectural applications, fall short of the demand for energy-efficient solutions due to their relatively high thermal conductivity, reported to be around 1 W m^{-1} K^{-1} (*27*). Conversely, Zr-DPA/EP demonstrates enhanced thermal insulation, showing a much lower thermal conductivity of 0.16 W m^{-1} K^{-1} (Fig. 5A). This result is attributed to the polymer chains with low phonon mean free range inherently contribute to low thermal conductivity. In addition, the molecular cages that maintain the porosity of MC-MOF within the polymer matrix introduce an abundance of microporous and mesoporous structures that effectively reflect and scatter phonons, thus mitigating lattice thermal conductivity. The well-defined interface between the polymer and

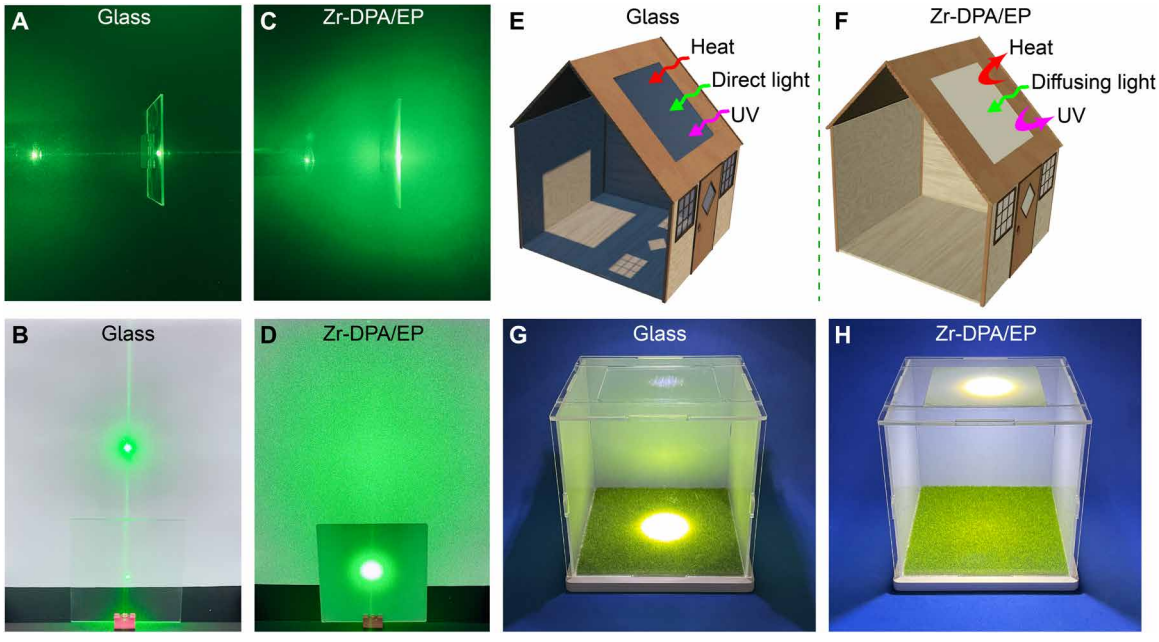

Fig. 4. Light management of MC-MOF/polymer. (**A**) Side view and (**B**) front view of laser irradiation of glass. (**C**) Side view and (**D**) front view of laser irradiation of Zr-DPA/EP. Schematic diagram of (**E**) glass and (**F**) Zr-DPA/EP as building materials. House model with (**G**) glass and (**H**) Zr-DPA/EP to simulate daylighting.

MC-MOF also enhances phonon scattering and increases interfacial thermal resistance, further elevating the thermal insulation.

To visually capture the disparities in thermal conductivity, infrared thermography images are taken over time, comparing glass and Zr-DPA/EP on a heating plate (Fig. 5B). In the case of glass, heat rapidly spreads from the edges to the center, achieving a uniform temperature distribution of 41°C within 1 min (Fig. 5, C and D, and fig. S18). Zr-DPA/EP, however, exhibits much slower heat diffusion, with a central temperature of approximately 36°C after 1 min. (Fig. 5, E and F, and fig. S19) The uneven temperature distribution visibly shows the exceptional thermal insulation capabilities of Zr-DPA/EP. Comparison of this work with previously reported epoxy-containing composites (*27*, *31*, *34*, *36*–*41*) in terms of thermal conductivity further reveals the excellent thermal insulation of Zr-DPA/EP (table S3).

Zr-DPA/EP, with its remarkable capabilities for light and heat management, has the potential to reduce energy consumption in buildings. We fabricate two models using glass or Zr-DPA/EP materials, with a black aluminum oxide block placed in the middle. They are placed outdoors to receive sunlight, and the temperature variations of the black block from 8 a.m. to 5 p.m. are recorded using an infrared camera (Fig. 5G). The temperature of the black block in the Zr-DPA/EP model consistently remains lower than that in the glass model (Fig. 5, H and I), indicating that Zr-DPA/EP, through scattering, induces a uniform light distribution, preventing direct sunlight exposure to the black block and slowing down heat transfer. This suggests that Zr-DPA/EP is conducive to maintaining a cool interior in tropical buildings.

We also conduct a comparative study on heating energy consumption from last November to this April in six cities located in cold regions. The results, depicted in Fig. 5 (J and K), reveal monthly energy savings, highlighting the difference between the heating energy demand of buildings using glass and those using Zr-DPA/EP. Typically, the most substantial savings are realized in January, with an average reduction of 6.6 MJ m^{-2}. Figure 5L provides a comprehensive overview of the total heating energy consumption, revealing that buildings incorporating Zr-DPA/EP consistently outperform their glass-equipped counterparts across all cities, with an average reduction in energy loss of 28 MJ m^{-2}. This suggests that Zr-DPA/EP holds great promise for sustainable energy management in diverse urban environments.

DISCUSSION

In this work, we develop an MC-MOF for impeding the molecule penetration in MOF-polymers. MC-MOF, exemplified by Zr-DPA,

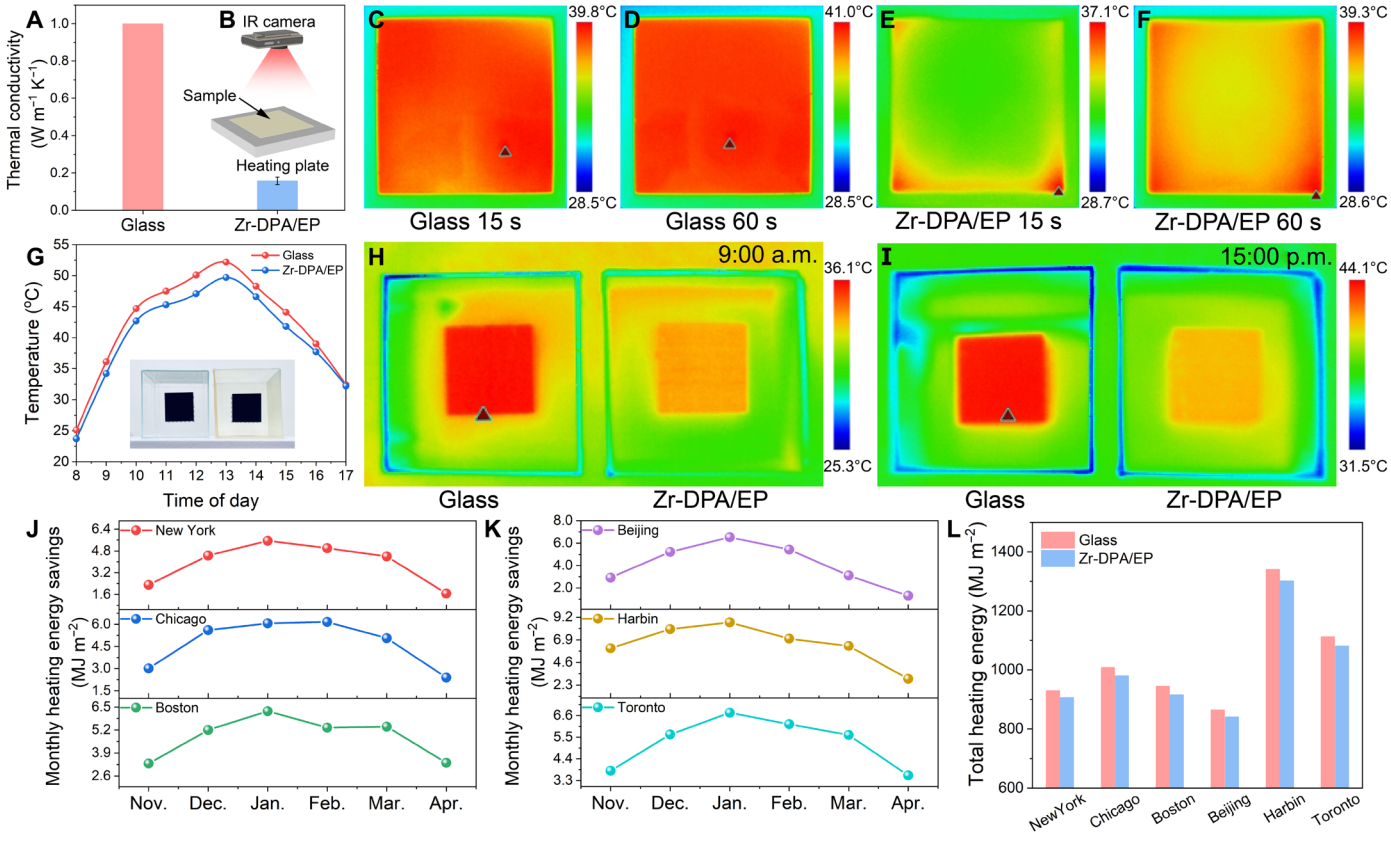

Fig. 5. Thermal management of MC-MOF/polymer. (**A**) Thermal conductivity of glass and Zr-DPA/EP. (**B**) Schematic diagram of an infrared (IR) thermal imaging camera monitoring the heat transfer process. Infrared thermal imaging of glass after (**C**) 15 s and (**D**) 60s on a hot plate. Infrared thermal imaging of Zr-DPA/EP after (**E**) 15 s and (**F**) 60s on a hot plate. (**G**) Temperature changes after solar irradiation of black blocks in glass or Zr-DPA/EP models. Temperature difference of the black block in the glass and Zr-DPA/EP models at (**H**) 9:00 a.m. and (**I**) 15:00 p.m. (**J**) Monthly heating energy savings of Buildings with Zr-DPA/EP in New York, Chicago, and Boston. (**K**) Monthly heating energy savings of Buildings with Zr-DPA/EP in Beijing, Harbin, and Toronto. (**L**) Comparison of total heating energy consumption of buildings using glass and Zr-DPA/EP in six cities.

exhibits promising potential for enhancing energy management in polymers. Zr-DPA/EP showcases efficient light harvesting capabilities, achieving an impressive haze of 93% while maintaining 83% transmittance with a mere 0.5 wt % loading of Zr-DPA. This composite also boasts broad UV shielding, UV fluorescence, and remarkable thermal insulation performance. Consequently, it contributes to the uniform lighting distribution and reduced energy consumption in sustainable architectural designs when compared to traditional glass materials. The innovative concept of engineering MC-MOFs with high porosity and tailored windows through ligand engineering offers a versatile approach to optimizing MOF performance in polymer matrices and also sparks additional possibilities for the application of MOF-polymer composites in sustainable energy.

MATERIALS AND METHODS

Materials

Zirconium chloride ($ZrCl_4$; 98%), TPDC (98%), DPA (99%), TFA (99%), MHHPA (99%), and 2,4,6-tris(dimethylaminomethyl)phenol (DMP-30; 95%) were purchased from Energy-Chemical. *N*,*N*-dimethylformamide (DMF; 99.5%) and methanol (99.5%) were supplied by Richjoint Co. Ltd., China. Diglycidyl ether of bisphenol A (DGEBA; technical grade) with the epoxy value of 0.51 was supported by Baling Petrochemical Co. Ltd., China.

Preparation of MOF (UiO-68 or Zr-DPA)

In the synthesis of UiO-68 or Zr-DPA, $ZrCl_4$ (23.3 mg), TPDC (ligand of UiO-68, 31.8 mg) or DPA (ligand of Zr-DPA, 41.8 mg), and TFA (100 μl) were dissolved by heating in a glass vial containing 20 ml of DMF. The glass vials were sealed and placed in an oven at 120°C for 24 hours. Subsequently, it was slowly cooled down to room temperature, and the resulting precipitate was subjected to multiple washes and centrifugations using DMF and methanol. UiO-68 or Zr-DPA was obtained after being dried in vacuum at 80°C.

Preparation of MOF-polymer composites

MOF (UiO-68 or Zr-DPA, 0.050 g), epoxy prepolymer DGEBA (E51, 5.332 g) and curing agent MHHPA (4.568 g) were stirred without solvent for 6 to 8 hours at room temperature to ensure that the MOF was uniformly dispersed in the epoxy system. Subsequently, the accelerator DMP-30 (0.050 g) was added, the mixture was degassed in a vacuum oven at 60°C to eliminate bubbles before being poured into a mold, and the epoxy prepolymer system was cured at 120°C. The optical sample thickness is 1 mm.

Characterizations

N_2 adsorption-desorption isotherms were achieved by a fully automated specific surface area and porosity analyzer (Micromeritics ASAP 2460). XRD was measured by an x-ray diffractometer (Bruker D8) from 3° to 50° (2θ). XRD simulations were performed on Mercury. FTIR spectra were tested on a Vertex70 spectrometer (Bruker) from 400 to 4000 cm^{-1}. The morphology of MOFs and the fracture surface of composites were observed by SEM (NOVA NANOSEM 430). MOF particle size was tested by a nanoparticle size analyzer (Malvern). According to ASTM D1003, optical properties are collected using a UV-visible spectrophotometer with an integrating sphere (Hitachi U-3900H) in the wavelength range of 300 to 800 nm. Haze is calculated using the following formula

$$\text{Haze} = \left(\frac{T_4}{T_2} - \frac{T_3}{T_1} \right) \times 100\,\%$$

where T_1 and T_3 are used for instrument calibration without samples in their transmission ports. T_1 has a white standard on its reflection port for testing the incident light, while T_3 has an open reflection port for measuring the light scattered by the instrument. T_2 and T_4 have samples in their transmission ports. T_2 has a white standard on its reflection port for measuring the total light transmittance of the sample. T_4 has an open reflection port for assessing the total light scattering of the sample and instrument.

Fluorescence emission spectra were tested by a fluorescence spectrometer (FluoroMax, Horiba) with an excitation wavelength of 360 nm. The thermal conductivity test of the samples was divided into three parts: thermal diffusion coefficient test, specific heat capacity test, and density test. The thermal diffusion coefficient (α) was tested by NETZSCH LFA 447 laser flash thermal conductivity tester. The samples were 12.7-mm-diameter discs with a thickness of about 1 mm. The surfaces of the samples were coated with graphite. The specific heat capacity was measured using a NETZSCH DSC204F1 differential scanning calorimeter. The heat flow values of the samples were measured at 30°C from −10° to 50°C with a rate of 10°C/min in N_2. Sapphire was used as the standard sample, and the specific heat capacity value of the sample was calculated according to the formula

$$C_{\text{p sam}} = \frac{Y_{\text{sam}} \times m_{\text{std}} \times C_{\text{p std}}}{Y_{\text{std}} \times m_{\text{sam}}}$$

where, $C_{\text{p sam}}$ and $C_{\text{p std}}$ were the sample and sapphire specific heat capacity values (J kg^{-1} K^{-1}), m_{sam} and m_{std} were the sample and sapphire mass (mg), Y_{sam} and Y_{std} are the heat flow values of sample and sapphire (mW). The density (ρ) was tested using a density balance of GF 300D from AND, Japan. The thermal conductivity (λ) was calculated in W m^{-1} K^{-1} according to the formula

$$\lambda = \alpha \times C_{\text{p sam}} \times \rho$$

Theoretical calculations

Connolly surface calculation

Single crystal data for MOF were sourced from Cambridge Crystallographic Data Center. The structural models of MOFs (UiO-68 and Zr-DPA) were established using BIOVIA Materials Studio. The Connoly surface was calculated by the Atom Volumes and Surfaces module, using a Connolly radius of 1.82 Å (N_2 kinetic diameter was 3.64 Å) and a grid interval of 0.15 Å.

Energy barrier calculation

The DFT calculations were carried out with the Vienna Ab initio Simulation Package (*42*). The Perdew-Burke-Ernzerhof functional within generalized gradient approximation was used to process the exchange-correlation (*43*). The projector augmented wave pseudopotential with a kinetic energy cutoff of 500 eV was used to describe the expansion of electronic eigenfunctions (*44*). The vacuum thickness was set to be 25 Å to minimize interlayer interactions. The Brillouin zone integration was sampled by a Γ-centered 1 × 1 × 1 Monkhorst-Pack k-point. All atomic positions were fully relaxed until energy and force reached a tolerance of 1×10^{-5} eV and 0.03 eV/Å, respectively. The DFT including dispersion corrections method was used to consider the long-range interactions (*45*). The minimum energy path for molecule diffusion and its corresponding

energy barrier were computed using the climbing image nudged elastic band method.

Energy consumption simulation

The energy consumption was calculated by EnergyPlus, and the building model used for the calculation was shown in fig. S20. Optical parameters of Zr-DPA/EP including solar transmittance, solar reflectance, visible transmittance, visible reflectance, and emissivity were listed in table S4, and the optical parameters of the glass are referenced from previous literature (*46*). Solar diffusing characteristics were added to Zr-DPA/EP. The six selected cities were located in the United States (New York, Chicago, and Boston), China (Beijing and Harbin), and Canada (Toronto), which were cold in winter with real heating needs and had large populations. Simulations focused on the period from last November to this April, as it requires more energy to regulate building temperatures in winter than in summer.

Supplementary Materials

This PDF file includes:

Figs. S1 to S20

Tables S1 to S4

REFERENCES AND NOTES

1. T. Kitao, Y. Zhang, S. Kitagawa, B. Wang, T. Uemura, Hybridization of MOFs and polymers. *Chem. Soc. Rev.* **46**, 3108–3133 (2017).
2. A. K. Bindra, D. Wang, Y. Zhao, Metal-organic frameworks meet polymers: From synthesis strategies to healthcare applications. *Adv. Mater.* **35**, (2023).
3. S. Yang, V. V. Karve, A. Justin, I. Kochetygov, J. Espin, M. Asgari, O. Trukhina, D. T. Sun, L. Peng, W. L. Queen, Enhancing MOF performance through the introduction of polymer guests. *Coord. Chem. Rev.* **427**, 213525 (2021).
4. D. Dai, H. Wang, C. Li, X. Qin, T. Li, A physical entangling strategy for simultaneous interior and exterior modification of metal–organic framework with polymers. *Angew. Chem. Int. Ed. Engl.* **133**, 7465–7472 (2021).
5. N. Hosono, T. Uemura, Metal-organic frameworks for macromolecular recognition and separation. *Matter* **3**, 652–663 (2020).
6. J. Lee, J. Lee, J. Y. Kim, M. Kim, Covalent connections between metal–organic frameworks and polymers including covalent organic frameworks. *Chem. Soc. Rev.* **52**, 6379–6416 (2023).
7. H. Wang, S. He, X. Qin, C. Li, T. Li, Interfacial engineering in metal–organic framework-based mixed matrix membranes using covalently grafted polyimide brushes. *J. Am. Chem. Soc.* **140**, 17203–17210 (2018).
8. S. Su, X. Zhou, X. Gong, K. B. Idrees, K. O. Kirlikovali, T. Islamoglu, O. K. Farha, N. C. Gianneschi, Metal–organic frameworks with a bioinspired porous polymer coating for sieving separation. *J. Am. Chem. Soc.* **145**, 13195–13203 (2023).
9. Z. Wang, W. Wang, T. Zeng, D. Ma, P. Zhang, S. Zhao, L. Yang, X. Zou, G. Zhu, Covalent-linking-enabled superior compatibility of ZIF-8 hybrid membrane for efficient propylene separation. *Adv. Mater.* **34**, e2104606 (2022).
10. M. Kalaj, K. C. Bentz, S. Ayala Jr., J. M. Palomba, K. S. Barcus, Y. Katayama, S. M. Cohen, MOF-polymer hybrid materials: From simple composites to tailored architectures. *Chem. Rev.* **120**, 8267–8302 (2020).
11. Z. Tang, W. Tress, O. Inganäs, Light trapping in thin film organic solar cells. *Mater. Today* **17**, 389–396 (2014).
12. F. J. Haug, C. Ballif, Light management in thin film silicon solar cells. *Energ. Environ. Sci.* **8**, 824–837 (2015).
13. A. Ghosh, Diffuse transmission dominant smart and advanced windows for less energy-hungry building: A review. *J. Build. Eng.* **64**, 105604 (2022).
14. H. Khandelwal, A. P. H. J. Schenning, M. G. Debije, Infrared regulating smart window based on organic materials. *Adv. Energy Mater.* **7**, 1602209 (2017).
15. T. Li, M. Zhu, Z. Yang, J. Song, J. Dai, Y. Yao, W. Luo, G. Pastel, B. Yang, L. Hu, Wood composite as an energy efficient building material: Guided sunlight transmittance and effective thermal insulation. *Adv. Energy Mater.* **6**, 1601122 (2016).
16. W. Wang, L. Qi, Light management with patterned micro- and nanostructure arrays for photocatalysis, photovoltaics, and optoelectronic and optical devices. *Adv. Funct. Mater.* **29**, 1807275 (2019).
17. C. R. Marshall, J. P. Dvorak, L. P. Twight, L. Chen, K. Kadota, A. B. Andreeva, A. E. Overland, T. Ericson, A. F. Cozzolino, C. K. Brozek, Size-dependent properties of solution-processable conductive MOF nanocrystals. *J. Am. Chem. Soc.* **144**, 5784–5794 (2022).
18. L. Feng, H. F. Drake, E. A. Joseph, H.-C. Zhou, From fundamentals to applications: A toolbox for robust and multifunctional MOF materials. *Chem. Soc. Rev.* **47**, 8611–8638 (2018).
19. X. Ye, D. Liu, Metal–organic framework UiO-68 and its derivatives with sufficiently good properties and performance show promising prospects in potential industrial applications. *Cryst. Growth Des.* **21**, 4780–4804 (2021).
20. Y. Bai, Y. Dou, L.-H. Xie, W. Rutledge, J.-R. Li, H.-C. Zhou, Zr-based metal–organic frameworks: Design, synthesis, structure, and applications. *Chem. Soc. Rev.* **45**, 2327–2367 (2016).
21. Z. Li, F. Jiang, M. Yu, S. Li, L. Chen, M. Hong, Achieving gas pressure-dependent luminescence from an AIEgen-based metal-organic framework. *Nat. Commun.* **13**, 2142 (2022).
22. J. Perego, C. X. Bezuidenhout, I. Villa, F. Cova, R. Crapanzano, I. Frank, F. Pagano, N. Kratochwill, E. Auffray, S. Bracco, Highly luminescent scintillating hetero-ligand MOF nanocrystals with engineered Stokes shift for photonic applications. *Nat. Commun.* **13**, 3504 (2022).
23. J. Xue, Y. Gu, Q. Shan, Y. Zou, J. Song, L. Xu, Y. Dong, J. Li, H. Zeng, Constructing mie-scattering porous interface-fused perovskite films to synergistically boost light harvesting and carrier transport. *Angew. Chem. Int. Ed.* **56**, 5232–5236 (2017).
24. Z. Hu, I. Castano, S. Wang, Y. Wang, Y. Peng, Y. Qian, C. Chi, X. Wang, D. Zhao, Modulator effects on the water-based synthesis of Zr/Hf metal–organic frameworks: Quantitative relationship studies between modulator, synthetic condition, and performance. *Cryst. Growth Des.* **16**, 2295–2301 (2016).
25. Q. Xia, C. Chen, T. Li, Solar-assisted fabrication of large-scale, patternable transparent wood. *Sci. Adv.* **7**, 7342 (2021).
26. Z. Wang, J. Gao, X. Wang, Y. Zhang, L. Cai, Optically transparent bamboo with magnetic properties. *Compos. Sci. Technol.* **230**, 109763 (2022).
27. R. Mi, C. Chen, T. Keplinger, Y. Pei, S. He, D. Liu, J. Li, J. Dai, E. Hitz, B. Yang, I. Burgert, L. Hu, Scalable aesthetic transparent wood for energy efficient buildings. *Nat. Commun.* **11**, 3836 (2020).
28. M. Zhu, J. Song, T. Li, A. Gong, Y. Wang, J. Dai, Y. Yao, W. Luo, D. Henderson, L. Hu, Highly anisotropic, highly transparent wood composites. *Adv. Mater.* **28**, 5181–5187 (2016).
29. M. Wu, J. Li, X. Zhang, S. Liu, J. Zhao, W. Xie, Design of imide oligomer-mediated MOF clusters for solar cell encapsulation systems by interface fusion strategy. *Adv. Sci.* **10**, e2206748 (2023).
30. K. Wang, Y. Dong, Z. Ling, X. Liu, S. Q. Shi, J. Li, Transparent wood developed by introducing epoxy vitrimers into a delignified wood template. *Compos. Sci. Technol.* **207**, 108690 (2021).
31. X. Wang, S. Shan, S. Q. Shi, Y. Zhang, L. Cai, L. M. Smith, Optically transparent bamboo with high strength and low thermal conductivity. *ACS Appl. Mater. Interfaces* **13**, 1662–1669 (2020).
32. S. Huo, Z. Zhou, J. Jiang, T. Sai, S. Ran, Z. Fang, P. Song, H. Wang, Flame-retardant, transparent, mechanically-strong and tough epoxy resin enabled by high-efficiency multifunctional boron-based polyphosphonamide. *Chem. Eng. J.* **427**, 131578 (2022).
33. Q. Shi, S. Huo, C. Wang, G. Ye, L. Yu, Z. Fang, H. Wang, Z. Liu, A phosphorus/silicon-based, hyperbranched polymer for high-performance, fire-safe, transparent epoxy resins. *Polym. Degrad. Stab.* **203**, 110065 (2022).
34. L. Zhang, A. Wang, T. Zhu, Z. Chen, Y. Wu, Y. Gao, Transparent wood composites fabricated by impregnation of epoxy resin and W-doped VO2Nanoparticles for application in energy-saving windows. *ACS Appl. Mater. Interfaces* **12**, 34777–34783 (2020).
35. G. Ye, S. Huo, C. Wang, P. Song, Z. Fang, H. Wang, Z. Liu, Durable flame-retardant, strong and tough epoxy resins with well-preserved thermal and optical properties via introducing a bio-based, phosphorus-phosphorus, hyperbranched oligomer. *Polym. Degrad. Stab.* **207**, 110235 (2023).
36. K. Wang, H. Peng, Q. Gu, X. Zhang, X. Liu, Y. Dong, Y. Cai, Y. Li, J. Li, Scalable, large-size, and flexible transparent bamboo. *Chem. Eng. J.* **451**, 138349 (2023).
37. C. Jia, C. Chen, R. Mi, T. Li, J. Dai, Z. Yang, Y. Pei, S. He, H. Bian, S.-H. Jang, J. Y. Zhu, B. Yang, L. Hu, Clear wood toward high-performance building materials. *ACS Nano* **13**, 9993–10001 (2019).
38. Y.-Y. Wang, F.-L. Guo, Y.-Q. Li, W.-B. Zhu, Y. Li, P. Huang, N. Hu, S.-Y. Fu, High overall performance transparent bamboo composite via a lignin-modification strategy. *Compos. Part B Eng.* **235**, 109798 (2022).
39. K. Wang, X. Liu, Y. Dong, Z. Ling, Y. Cai, D. Tian, Z. Fang, J. Li, Editable shape-memory transparent wood based on epoxy-based dynamic covalent polymer with excellent optical and thermal management for smart building materials. *Cellul.* **29**, 7955–7972 (2022).
40. Y. Liu, X. Liu, L. Li, M. Wang, J. Hou, Y. Wu, Y. Ma, S. Luo, Y. Wu, Y. Qing, Inspired by chromophores: A intelligent transparent bamboo with intrinsic photo- and pH-responsiveness. *Ind. Crops. Prod.* **203**, 117206 (2023).
41. G. G. Kaya, E. Yilmaz, H. Deveci, Sustainable nanocomposites of epoxy and silica xerogel synthesized from corn stalk ash: Enhanced thermal and acoustic insulation performance. *Compos. Part B Eng.* **150**, 1–6 (2018).

42. G. Kresse, J. Furthmüller, Efficiency of ab-initio total energy calculations for metals and semiconductors using a plane-wave basis set. *Comput. Mater. Sci.* **6**, 15–50 (1996).
43. J. P. Perdew, K. Burke, M. Ernzerhof, Generalized gradient approximation made simple. *Phys. Rev. Lett.* **77**, 3865–3868 (1996).
44. P. E. Blöchl, Projector augmented-wave method. *Phys. Rev. B* **50**, 17953 (1994).
45. S. Grimme, Semiempirical GGA-type density functional constructed with a long-range dispersion correction. *J. Comput. Chem.* **27**, 1787–1799 (2006).
46. W. Guo, L. Kong, T. Chow, C. Li, Q. Zhu, Z. Qiu, L. Li, Y. Wang, S. B. Riffat, Energy performance of photovoltaic (PV) windows under typical climates of China in terms of transmittance and orientation. *Energy* **213**, 118794 (2020).

Acknowledgments: We thank the High-Performance Computing Center of Central South University for providing computing resources. We thank X. Yu, H. Chen, and L. Li for assistance in sample preparation and thermal conductivity testing. **Funding:** This work was supported by the National Natural Science Foundation of China (52303117). **Author contributions:** Conceptualization: M.W. and W.X. Methodology: M.W. and W.X. Investigation: M.W., G.L., R.L., and X.L. Visualization: M.W. Supervision: W.X., J.Z., and S.L. Writing—original draft: M.W. and W.X. Writing—review and editing: J.Z. and W.X. **Competing interests:** The authors declare that they have no competing interests. **Data and materials availability:** All data needed to evaluate the conclusions in the paper are present in the paper and/or the Supplementary Materials.

Submitted 18 October 2023
Accepted 4 April 2024
Published 8 May 2024
10.1126/sciadv.adl4449